Coupled-channels analysis of ^{58}Ni+^{124}Sn reactions

H. Esbensen, C. L. Jiang, and K. E. Rehm
Physics Division, Argonne National Laboratory, Argonne, Illinois 60439
(Received 11 December 1997)

Measurements of multineutron transfer reactions in ^{58}Ni+^{124}Sn collisions are analyzed in a simplified coupled-channels model. Successive one-neutron and direct two-neutron transfer couplings are included explicitly, together with 2^+ and 3^- excitations of projectile and target. Capture reactions, i.e., fusion and deep-inelastic reactions, are described by ingoing-wave boundary conditions. Quasielastic charged-particle transfer reactions are not treated explicitly but are simulated by a weak imaginary potential. The model provides a comprehensive description of the measured reaction and elastic scattering data, from far below to well above the Coulomb barrier. We find that subbarrier capture rates are enhanced by couplings to neutron transfer channels but the enhancement is not as large as caused by couplings to low-lying surface modes. [S0556-2813(98)04205-8]

PACS number(s): 24.10.Eq, 25.70.Bc, 25.70.Hi, 25.70.Jj

I. INTRODUCTION

Complete measurements of all reaction channels in heavy-ion collisions over a wide range of beam energies, from far below to well above the Coulomb barrier, are available only for a few systems. One example is ^{58}Ni+^{124}Sn. Here measurements of fusion-evaporation residues [1], fusion-fission [2,3], and deep-inelastic reactions [3] have been available for some time. Single-neutron transfer data exist down to energies far below the Coulomb barrier [4,5]. One- and two-neutron transfers, as well as elastic scattering and charged-particle transfers, have also been measured well above the Coulomb barrier [6,7]. Recently, multinucleon, in particular multineutron, transfer data have become available at energies close to the Coulomb barrier [8].

All these data present a challenge to theory, and it is of interest to try to develop a model that can account for the data in a single, consistent calculation. This is quite difficult in a coupled-channels approach because of the large number of channels that are involved, not only with respect to the number of mass partitions but also with respect to the broad Q-value distributions that have been observed for each mass partition [8].

One model that has been applied successfully to heavy-ion reactions at energies well above the Coulomb barrier is based on semiclassical theory [9]. The model has, however, some difficulties at energies near and below the Coulomb barrier, where quantal tunneling plays an important role for the fusion of the two systems. In this paper we adopt a coupled-channels approach. To make it feasible we have to restrict the number of channels that can be included and limit these to ≈ 20.

The model we use was developed earlier to analyze fusion data for different nickel isotopes [10]. These fusion data [11] exhibit an isotope anomaly with an unexpected large enhancement for the ^{58}Ni+^{64}Ni system, which could only be explained by postulating a direct two-neutron transfer coupling [10]. The model that was developed reproduced the one-neutron transfer and the inclusive elastic scattering data that had been measured slightly above the Coulomb barrier. It also predicted surprisingly well the pure elastic scattering data that were measured later [12].

The two-neutron transfer data that now have become available for the system ^{58}Ni+^{124}Sn [8] allow us to calibrate the direct two-neutron transfer coupling more accurately, and the issue concerning the influence of transfer reactions on subbarrier fusion, which has often been debated in the literature (see, for example, Ref. [6]), can therefore be addressed with some confidence.

In the next section we present the assumptions made for our coupled-channels calculations and discuss how the pair-transfer coupling is calibrated. Detailed comparisons to neutron transfer data are presented in Sec. III. Elastic scattering and absorption cross sections are discussed in Sec. IV. Finally, we discuss in Sec. V the enhancement of subbarrier fusion that our model predicts.

II. SIMPLIFIED COUPLED-CHANNELS APPROACH

The framework of the coupled-channels calculations that we have performed is described in detail in Ref. [10]. It is based on the rotating frame approximation which allows us to reduce the number of channels for each inelastic excitation (or single-nucleon transfer) of multipolarity λ, from $\lambda+1$ to one effective channel. Here we include the four channels associated with the excitation of the lowest 2^+ and 3^- states in the two reacting nuclei. In our calculations of fusion presented in Sec. V we also include two-phonon and mutual excitations.

The excitation of the 2^+ and 3^- states is generated by Coulomb and nuclear vibrational couplings as described in [13]. The coupling strengths can be characterized by the amplitudes $\sigma_{n\lambda} = \beta_{n\lambda}R/\sqrt{4\pi}$, and the values we have used are quoted in Table I. The Coulomb excitation is calculated to first order in these amplitudes, whereas the nuclear couplings are calculated to second order (see Appendix A of Ref. [13]).

A. Ion-ion potential and absorption

The ion-ion potential that we use is given by

$$U(r) = \frac{V_0}{1+\exp\,[(r-R_0)/a]}, \tag{1}$$

TABLE I. Excitation energies and coupling strengths $\sigma_{n\lambda}$ for the Coulomb (Cou) and nuclear (nuc) excitation of the lowest 2^+ and 3^- states. The Coulomb coupling strengths have been determined from known $B(E\lambda)$ values. The nuclear coupling strengths for ^{58}Ni are from Ref. [14], whereas those for ^{124}Sn have been set equal to the Coulomb coupling strengths.

Nucleus	λ^π	$\Delta E_{n\lambda}$ (MeV)	$B(E\lambda)$ (e^2 b$^\lambda$)	$\sigma_{n\lambda}^{\mathrm{Cou}}$ (fm)	$\sigma_{n\lambda}^{\mathrm{nuc}}$ (fm).
^{58}Ni	2^+	1.45	0.068	0.24	0.28
	3^-	4.47	0.019	0.27	0.27
^{124}Sn	2^+	1.13	0.166	0.16	0.16
	3^-	2.61	0.073	0.18	0.18

where $V_0=-84.35$ MeV, $a=0.687$ fm, and $R_0=10.59$ fm. This is close to the empirical interaction of Ref. [15] [see their Eqs. (40),(41) and (44),(45) in Chap. III.1] but the total radius R_0 has been increased by 0.14 fm so that we get a realistic description of the measured subbarrier fusion (see Sec. V). The Coulomb barrier height produced by this potential is $V_{\mathrm{CB}}=158.5$ MeV. It is noted that this barrier height is slightly lower than the 160.2 MeV obtained from the real part of the optical potential which was used in Ref. [8] to describe the elastic scattering of ^{58}Ni+^{124}Sn.

Ideally, we would like to include couplings to all excitation and transfer channels that are populated in the experiments. One set of reactions that it would be difficult to include is deep-inelastic reactions because they involve multiple excitations and transfers. In a semiclassical picture, they originate from trajectories that overcome the barrier in the entrance channel but somehow manage to escape before a compound nucleus is formed. A simple way to include them in a coupled-channels calculation, which is based on a restricted number of channels, is to consider them, together with fusion reactions, as a part of a capture cross section. We adopt this view and simulate the capture processes by ingoing-wave boundary conditions. These boundary conditions are applied to all channels that are included explicitly, and they are imposed at the local minimum of the Coulomb plus nuclear potential inside the Coulomb barrier.

Our coupled-channels calculations include explicitly the excitation of the lowest 2^+ and 3^- states in projectile and target, and up to three-neutron transfer channels as described in more detail in the next subsection. We ignore couplings to charged-particle transfer channels, partly because of limitations on the number of channels that we can handle, and partly because these channels are considerably weaker than the neutron transfer channels.

It is useful, however, to have a realistic total reaction cross section when calculating observables like angular distributions for elastic scattering and for one- and two-neutron transfer. In such calculations we shall therefore employ, in addition to the ingoing-wave boundary condition, a weak imaginary potential of the form

$$W(r)=\frac{i\ \ W_0}{1+\exp\left[(r-R_0)/a\right]}. \tag{2}$$

Here we use for simplicity the same radius and diffuseness as used in the ion-ion potential. The strength W_0 is adjusted so that the total absorption cross section, generated by this imaginary potential and by the ingoing-wave boundary conditions, reproduces the sum of the measured fusion, deep-inelastic, and quasielastic, charged-particle transfer cross sections. In Sec. IV we show that this is achieved for $W_0=-7$ MeV. It is noted that this imaginary potential is much weaker than the one used in Ref. [8]. The main reason is that we employ ingoing-wave boundary conditions, which account for much of the absorption, whereas the calculations performed in Ref. [8] were based on solutions that have regular boundary conditions at the origin.

We shall always include this imaginary potential in our calculations, except when calculating capture cross sections; the imaginary potential is then set equal to zero, in order to isolate the capture rate from the total absorption.

TABLE II. Spectroscopic information [16,17] for the reaction ^{124}Sn(^{58}Ni,^{59}Ni)^{123}Sn used to calculate the form factors [18], which contain the normalization factors $A\cdot N$. The neutron separation energies of ^{124}Sn and ^{59}Ni are 8.488 and 9.000 MeV, respectively.

^AZ	(l,j)	E^* (MeV)	S	$A\cdot N$
^{123}Sn	$h_{11/2}$	0.000	4.50	13.6
	$d_{3/2}$	0.020	3.00	14.9
	$s_{1/2}$	0.139	1.90	15.6
	$d_{5/2}$	1.325	6.00	13.8
^{59}Ni	$p_{3/2}$	0.000	0.59	10.5
	$f_{5/2}$	0.339	0.71	9.2
	$p_{1/2}$	0.465	0.52	10.3
	$p_{3/2}$	0.878	0.10	10.5

B. Successive single-neutron transfers

The single-neutron transfers considered here include transitions from the four lowest $h_{11/2}$, $d_{3/2}$, $s_{1/2}$, and $d_{5/2}$ hole states in ^{123}Sn to the four lowest $p_{3/2}$, $f_{5/2}$, $p_{1/2}$, and $p_{3/2}$ particle states in ^{59}Ni. The spectroscopic factors for ^{123}Sn were taken from (p,d) measurements on ^{124}Sn [16], whereas those associated with ^{59}Ni were taken from (d,p) measurements on ^{58}Ni [17]. We use the simple parametrization of one-neutron transfer form factors developed by Quesada *et al.* [18]. All that is required to generate them are the spectroscopic factors, the single-particle binding energies in the initial or final states, and the normalization factors $A\cdot N$ of the associated wave functions. The relevant values are quoted in Table II.

All of these one-neutron transfer processes generate a Q-value distribution that is reasonably narrow and located close to $Q\approx 0$. This was confirmed by coupled-channels calculations performed in the rotating frame approximation [10], including all 16 transfer channels associated with the four initial and four final states mentioned above. At $E_{\mathrm{c.m.}}=150$ MeV, the average Q value was -0.3 MeV, with a spread of 0.7 MeV. The small spread in the calculated one-neutron transfer Q values allows us to combine all these transfers into one effective channel with the Q value $Q_{1n}=-0.3$ MeV and the effective form factor

$$F_{1n}(r)=F_{\mathrm{cal}}\ \sqrt{\sum_{\beta\lambda}\ |F_{\beta\lambda}(r)|^2}. \tag{3}$$

Here $F_{\beta\lambda}(r)$ are the form factors for the 16 individual transfer channels (β) mentioned above, with different multipolarities λ. Only a slight scaling of this form factor, F_{cal} = 0.955, was required to reproduce the more detailed calculation which included all 16 transfer channels.

In order to describe multineutron transfers as a successive process, we need to specify the effective form factors and Q values for the successive steps of single-neutron transfers. Here we assume for simplicity that the radial form of these form factors is the same as in the first step. Moreover, we truncate the calculations at the three-neutron ($3n$) transfer channel and set the Q values for the $2n$ and $3n$ channels equal to the -0.3 MeV that we adopted for the $1n$ channel. To fix the strength of the effective coupling between the $1n$ and $2n$ channels and between the $2n$ and $3n$ channels, we use the empirical results of Ref. [19] which show that the cross section for one-neutron transfer is determined by a Gaussian integral over the Q-value window, from the ground state Q value Q_{gg} to $-\infty$. We therefore expect that the $1n$ transfer cross section in ^{59}Ni+^{123}Sn collisions (Q_{gg}= +5.44 MeV) is about twice the $1n$ transfer cross section in ^{58}Ni+^{124}Sn collisions (Q_{gg}=+0.51 MeV). We can simulate this expectation in our coupled channels calculations for ^{58}Ni+^{124}Sn by adopting the effective coupling

$$F_{2n,1n}(r)=\sqrt{2}\times F_{1n}(r) \tag{4}$$

between the $1n$ and $2n$ transfer channels. The form factor that couples the $2n$ and $3n$ transfer channels is more uncertain and we have made the somewhat arbitrary choice

$$F_{3n,2n}(r)=\sqrt{3/2}\times F_{1n}(r). \tag{5}$$

In the comparison to data we shall therefore emphasize the results for the $1n$ and $2n$ transfers.

A schematic diagram of the coupling scheme we use is shown in Fig. 1. We assume that inelastic excitation and transfer are two independent degrees of freedom and adopt the same set of excited states and coupling strengths (given in Table I) for each mass partition. We also assume that single-neutron transfer can take place from any excited state in a given mass partition to the same excited state in the neighboring mass partitions.

A useful way to present the angular distributions for the various multineutron transfer channels, $d\sigma_{xn}/d\Omega$, is to plot them relative to the inclusive elastic scattering $d\sigma'_{\text{el}}/d\Omega$ (which includes the elastic and inelastic scattering),

$$P_{xn}=\frac{d\sigma_{xn}}{d\Omega}\Bigg/\frac{d\sigma'_{\text{el}}}{d\Omega}, \tag{6}$$

as function of the distance of closest approach, D, in pure Coulomb scattering,

$$D=\frac{Z_1Z_2e^2}{2E_{\text{c.m.}}}\left(1+\frac{1}{\sin(\theta_{\text{c.m.}}/2)}\right). \tag{6'}$$

This ratio represents, to some extent, a transfer probability. If the transfer is a direct process, the falloff at large distances will primarily be determined by the square of the associated form factor. We shall not pursue the exact relationship here but refer to Ref. [5].

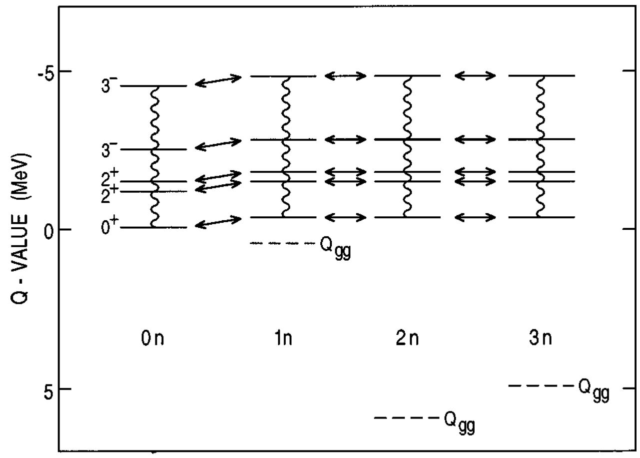

FIG. 1. Schematic illustration of the channels and couplings that are included in the coupled-channels calculations discussed in Sec. II B. Excitation and single-neutron transfer are assumed to be independent processes. Each mass partition (xn) (i.e., $^{58+x}$Ni + $^{124-x}$Sn, with x=0,1,2 and 3) has five states which are coupled by vibrational couplings as illustrated by the wiggly lines. Successive one-neutron transfer couplings between similar states in neighboring mass partitions are illustrated by double-headed arrows. The dashed lines show the ground state Q values Q_{gg}.

The one- and two-neutron transfer data obtained in Ref. [8] at the four energies $E_{\text{c.m.}}$=150, 153, 157, and 160.6 MeV are all plotted in this way both in Figs. 2(a) and 2(b). It is seen that the data cluster around a common curve, one for $1n$ transfer and a somewhat steeper curve for $2n$ transfer. The two figures also show the results of calculations, which were performed at the same four energies as discussed below, and they are seen to exhibit the same feature. This way of plotting the data is therefore quite useful when testing or calibrating the transfer form factors.

In Fig. 2(a) we show the results of calculations which included the successive neutron transfer couplings described above and also couplings to the 2^+ and 3^- states. To reproduce the $1n$ transfer data it was necessary to readjust the calibration factor in Eq. (3) to F_{cal} = 0.81. We do not quite understand why this reduction is necessary, except that it may reflect a model dependence of the spectroscopic factors. We note that such a reduction was not needed in the analysis of the neutron transfer in ^{58}Ni+^{64}Ni collisions [10].

With this adjustment of the one-neutron transfer form factor, there appears to be a fairly good agreement with the $1n$ transfer data, except at the smallest distances, where absorption starts to play an important role. While the $2n$ transfer data also exhibit an exponential falloff at large distances, the slope is clearly less steep than predicted by the calculations. We take this as evidence for a direct pair-transfer coupling. Another hint that pair transfer may play a role is the fact that the measured $2n$ transfer cross sections are always enhanced compared to the average exponential dependence of neutron transfer cross sections on the number of transferred neutrons; cf. Fig. 7 of Ref. [8].

C. Direct pair-transfer coupling

A simple way to fix the above discrepancy for the two-neutron transfer is to include in addition a direct pair-transfer coupling of the form

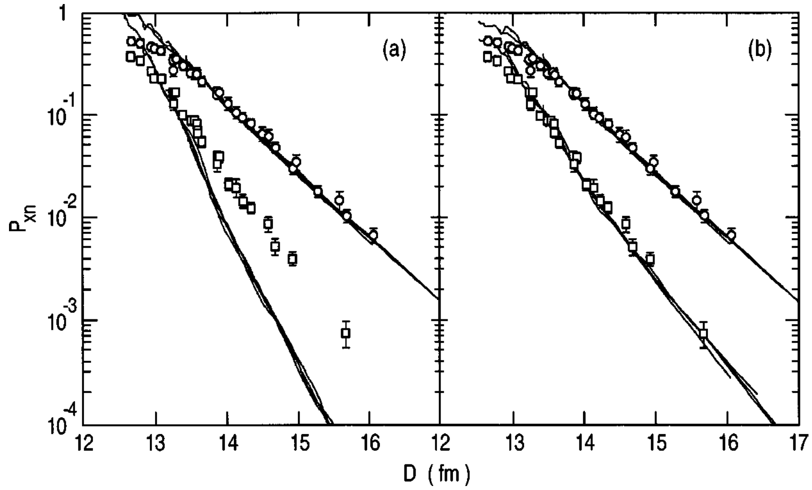

FIG. 2. Probabilities, as defined in Eq. (6), for the transfer of one neutron (open circles) and two neutrons (squares), as functions of the distance of closest approach in pure Coulomb scattering. The data points are from four different measurements [8], at $E_{\mathrm{c.m.}}$ = 150, 153, 157, and 160.6 MeV. The curves are the results of calculations performed at the same four energies, including excitations of the 2^+ and 3^- states and successive neutron transfer couplings (a) and including in addition the direct pair-transfer coupling (b).

$$F_{2n}(r)=\alpha_{2n}V_0\frac{d}{dr}\left[1+\exp\left(\frac{r-R_0}{a_{2n}}\right)\right]^{-1}. \tag{7}$$

It has a form that is similar to a nuclear excitation form factor, as proposed in the model by Dasso *et al.* [20]. The V_0 and R_0 are here the same as in the ion-ion potential (1), but the strength α_{2n} and the diffuseness a_{2n} will be adjusted.

We include this coupling between the $0n$ and $2n$ channels and also between the $1n$ and $3n$ channels. This is done similarly to the way we included the the one-neutron transfer couplings, namely, by assuming that pair-transfer and vibrational excitations are two independent degrees of freedom. A reasonable fit to the data can be achieved for α_{2n} = 0.04 fm and a_{2n} = 1.1 fm. The result is shown in Fig. 2(b). The uncertainty in the fit with respect to the diffuseness is about 10%. By comparing Figs. 2(a) and 2(b) it is seen that the calculated one-neutron transfer probability is insensitive to the additional pair-transfer coupling, except at the smallest distances.

In the following we shall always include this pair-transfer coupling in our calculations. It is actually a fairly weak coupling, since the strength α_{2n} is much smaller that the corresponding nuclear coupling strengths $\sigma_{n\lambda}^{\mathrm{nuc}}$, which are shown in Table I. However, the larger diffuseness makes it possible to generate a significant cross section. It is noted that the diffuseness a_{2n} = 1.1 fm is surprisingly large compared to the value of 0.85 fm that one would estimate from the two-neutron separation energy of ^{124}Sn.

III. COMPARISON TO NEUTRON TRANSFER DATA

Having calibrated the ion-ion potential, Eqs. (1) and (2), the single-neutron transfer form factors, Eqs. (3)–(5) with F_{cal} = 0.81, and the pair-transfer form factor, Eq. (7), we now present a more conventional comparison to the data of Ref. [8]. Since we truncate our calculations at the $3n$ transfer channel, we compare the calculated results for the $3n$ channel to the sum of the measurements of the $3n$, $4n$, $5n$, and $6n$ transfers. The results obtained at the lowest and the highest center-of-mass energies (150 and 160.6 MeV) are shown in Figs. 3(a) and 3(b), respectively.

The angular distributions shown in Fig. 3(a) peak at 180° as expected, since the energy is below the predicted Coulomb barrier, V_{CB} = 158.5 MeV. The $1n$ data point at 180° is from Refs. [4,5], and it is seen to be consistent with the measurements of Ref. [8], which cover the angular range of $98°-160°$. At the highest energy [Fig. 3(b)] absorption plays an important role and reduces the cross sections for head-on collisions. In fact, the absorption alone [i.e., from the imaginary potential (2) combined with ingoing-wave boundary conditions] reduces the angular distributions substantially at 180°. This is illustrated in Fig. 4, where the couplings to the 2^+ and 3^- states were turned off. When the couplings to inelastic excitations are turned on, as illustrated in Fig. 3(b), this reduction is weakened and smeared out.

The calculated curves shown in Figs. 3(a) and 3(b) are seen to trace the $1n$ and $2n$ transfer data quite well. The calculated $3n$ transfer is higher than the data at the highest energy, in spite of the fact that the data also include the measured $4n$, $5n$, and $6n$ transfers. We shall not try to fix this discrepancy because the modeling of such higher-order processes is very uncertain in a restricted coupled-channels treatment.

A comparison to the angle-integrated cross sections is shown in Fig. 5. The dashed curves do not include the effect of couplings to inelastic excitations whereas the solid curves do. It is seen that the solid curves make a smoother transition from below to above the Coulomb barrier, at least for the $2n$ and $3n$ transfers.

The solid points in Fig. 5 are the transfer data that were measured at energies well below the Coulomb barrier [4,5]. These cross sections were actually extracted from 180° scattering measurements by making a distorted-wave Born approximation (DWBA) analysis [4,5]. The extracted cross section at 150 MeV is 25% below the measurement of Ref. [8], performed at almost the same energy. This is somewhat surprising because the 180° measurement [4,5] is consistent with the angular distribution measured in Ref. [8], as illus-

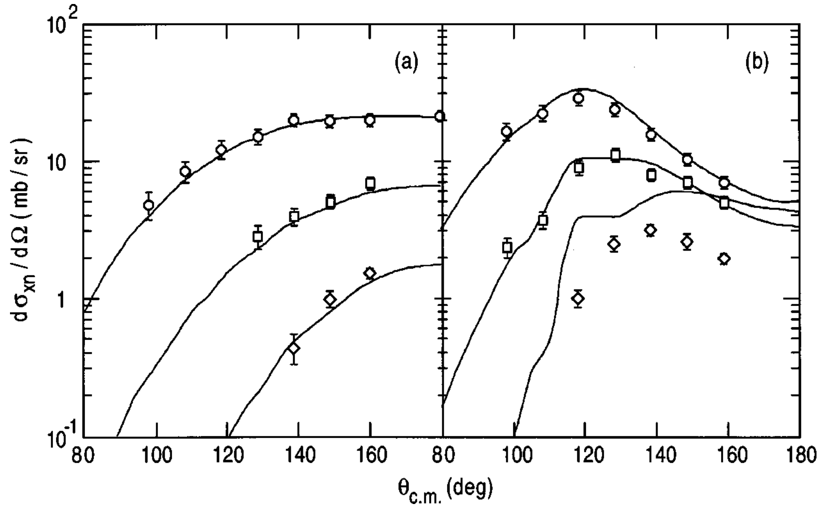

FIG. 3. Measured angular distributions (in decreasing order) for $1n$, $2n$, and the sum of $3n$ up to $6n$ transfer reactions [8] are shown at 150 MeV (a), and at 160.6 MeV (b). The curves are the corresponding calculated distributions. The data point in (a) at 180° is from Refs. [4,5].

trated in Fig. 3(a), and both measurements are reproduced quite well by our calculated angular distribution. The discrepancy is possibly due to the DWBA analysis [4,5], which may not simulate the actual absorption so well at this particular center-of-mass energy.

The extracted $1n$ cross sections shown in Fig. 5 are also smaller than calculated at energies far below the Coulomb barrier. Since the absorption should become insignificant here, a DWBA analysis should also become much more reliable. The differential cross sections that we calculate for 180° scattering are shown in Fig. 6, and they are in better agreement with the data. These features reflect the fact that the rotating frame approximation, which we make use of, is quite accurate at 180° but the total cross section is too large when the Q value is small (cf. Fig. 1 in Ref. [10]).

The calculated cross sections shown in Fig. 5 stay fairly constant above the Coulomb barrier and they are in reasonable agreement with measurements at $E_{c.m.}=168$ MeV [6] and 225 MeV [7]. A comparison to the $1n$ and $2n$ angular distributions measured at 225 MeV is shown in Fig. 7. The data points were generated from the Gaussian fit parameters that were published. The agreement with our calculations is surprisingly good, considering the limited number of channels we include in our coupled-channels calculations. The behavior at forward angles is difficult to judge because the actual measurements would show a rise due to deep-inelastic scattering [7]. The figure also shows that the elastic scattering data are consistent with our model calculation.

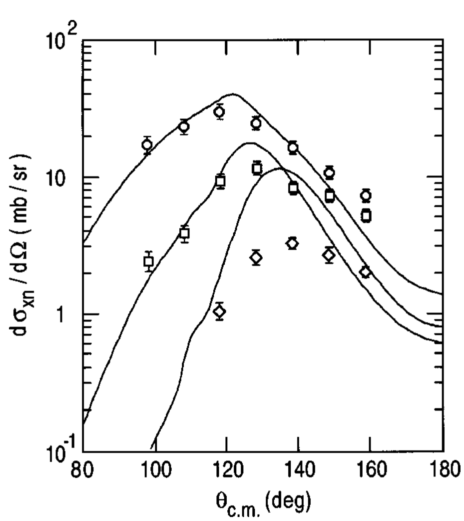

FIG. 4. Similar to Fig. 3(b) but without the effect of couplings to the 2^+ and 3^- excited states.

IV. ELASTIC SCATTERING AND ABSORPTION

The inclusive elastic scattering data [8] (i.e., elastic plus inelastic events with excitation energies up to 6 MeV) that were measured at four beam energies near the Coulomb barrier are show in Fig. 8. The dashed curves are the results we

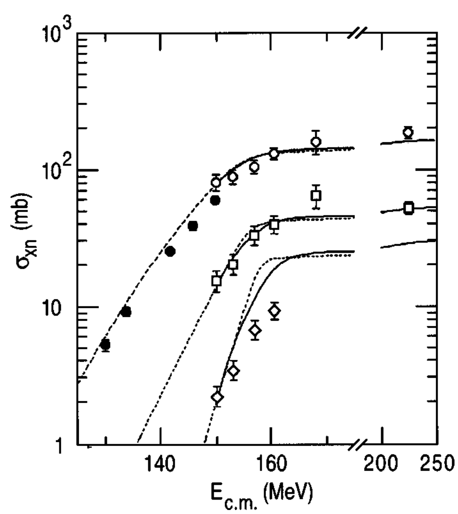

FIG. 5. Total $1n$, $2n$, and $3n$ cross sections are shown (in decreasing order) as functions of the center-of-mass energy. The dashed curves were obtained without any couplings to surface excitations, whereas the solid curves include the effect of these couplings. The low-energy $1n$ data (solid points) are from Refs. [4,5], and data at 168 and 225 MeV are from Refs. [6,7], respectively. The data between 150 and 160.6 MeV are from [8].

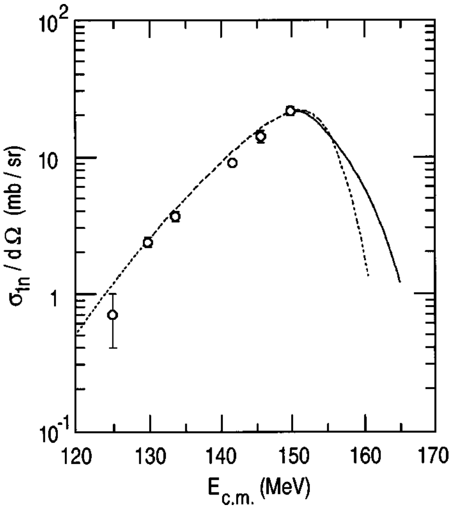

FIG. 6. Differential cross section for $1n$ transfer at 180°, as a function of the center-of-mass energy. The data are from Refs. [4,5]. The dashed curve was obtained without any couplings to surface modes, whereas the solid curve includes the effect of these couplings.

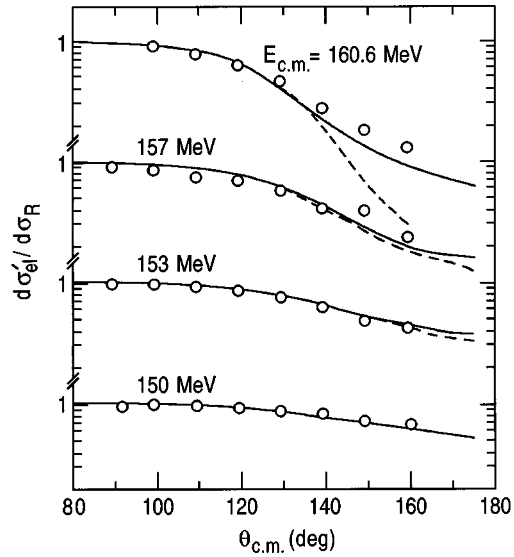

FIG. 8. The inclusive elastic scattering data (relative to Rutherford scattering) measured at $E_{\mathrm{c.m.}} = 150$ and 160.6 MeV [8] are compared to the results of the full calculations (solid curves). The dashed curves show the elastic scattering cross sections obtained when the couplings to the 2^+ and 3^- states are neglected.

obtain when we include only the couplings to the neutron transfer channels in our coupled-channels calculations. The solid curves are the inclusive elastic scattering distributions we obtain when we also include the excitation of the 2^+ and 3^- states in projectile and target. They are seen to trace the data quite well, except at the highest beam energy, where the calculated distribution is below the data at the largest scattering angles.

The solid and dashed curves in Fig. 8 are almost identical at the lowest beam energies but inelastic excitations, which are included in the solid curves, are seen to enhance the inclusive elastic scattering at the highest beam energies and largest scattering angles. A similar trend was seen in the calculated distributions for neutron transfer, where couplings to the 2^+ and 3^- states clearly enhanced the cross sections at large scattering angles [compare Figs. 3(b) and 4]. The discrepancy in Fig. 8 between the data and the solid curve at the highest beam energy may therefore partly be due to the fact that we have neglected certain excitations in our calculations, such as two-phonon and mutual excitations of the 2^+ and 3^- states. We shall see in the next section that such excitations have a significant influence on the subbarrier capture rate.

The absorption cross section that our model produces (from the imaginary potential combined with the ingoing-wave boundary conditions) is shown by the solid curve in Fig. 9, as a function of the center-of-mass energy. It is to be compared, as discussed in Sec. II, to the sum of the measured

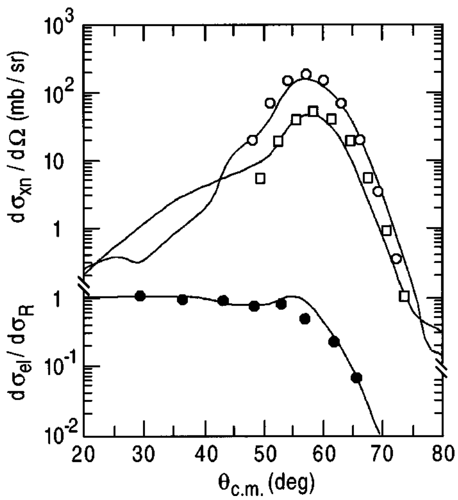

FIG. 7. Angular distributions for the $1n$ (open circles) and $2n$ transfer (squares) reactions measured at 225 MeV [7]. Also shown is the elastic scattering relative to the Rutherford cross section (solid points). The solid curves are the results of our coupled-channels calculations.

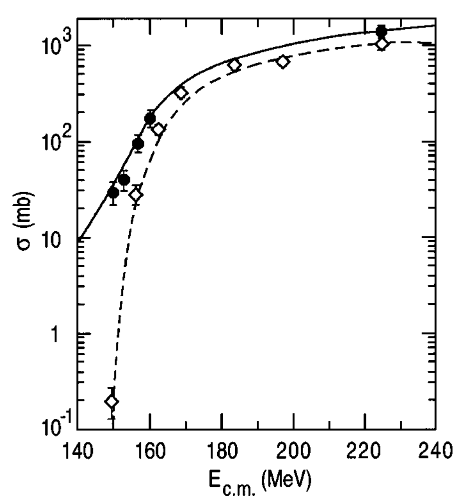

FIG. 9. Cross sections of fusion plus deep-inelastic scattering (open diamonds, from Refs. [1,3,7]) are compared to the calculated capture cross section (dashed curve). The solid points, which include in addition the measured quasielastic, charged-particle transfer cross sections [7,8], are compared to the calculated absorption cross section (solid curve).

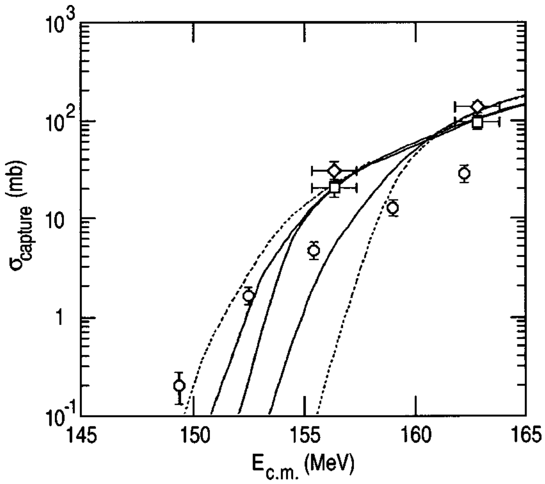

FIG. 10. Calculated capture cross sections are compared to the data for evaporation residues [1] (open circles), fusion [3] (squares), and fusion plus deep-inelastic reactions [3] (diamonds). The lowest dashed curve is the result of the one-dimensional barrier penetration. The three solid curves show in increasing order the separate effects of couplings to neutron transfer channels and to the low-lying 2^+ and 3^- states in projectile and target, and finally the combined effect of these two sets of couplings. The upper dashed curve includes, in addition, the effect of mutual excitations of 2^+ and 3^- states and two-phonon excitations of the 2^+ states.

fusion, deep-inelastic, and quasielastic, charged-particle transfer cross sections, which is shown by the solid points in Fig. 9. The depth of the imaginary potential was, in fact, adjusted to reproduce this sum at 160.6 MeV. This calibration is seen to make a very good prediction at 225 MeV, where the measured quasielastic, charged-particle transfer cross section was 386±54 mb, and the fusion and deep-inelastic cross sections were estimated to be 700 and 360 mb, respectively [7].

The dashed curve in Fig. 9 is the calculated capture cross section. It represents our most ambitious calculation which is discussed in the next section. It simulates, as discussed earlier, the sum of the measured fusion and deep-inelastic cross sections [1,3], which is indicated by the open symbols.

V. FUSION OR CAPTURE REACTIONS

Since our model describes fairly well many of the reaction data that have been obtained in ^{58}Ni+^{124}Sn collisions, it is now interesting to see the effects of the various couplings on the subbarrier fusion (or capture) enhancement and, in particular, to compare the effects of inelastic excitations and neutron transfers.

The results of various capture calculations are shown in Fig. 10. They were performed by setting the imaginary potential (2) equal to zero. The data shown are the evaporation residue cross sections (open circles) [1], the fusion cross section (squares) obtained by adding the measured fission cross sections [3], and finally the capture cross sections (diamonds) obtained by also including the deep-inelastic cross sections [3]. Here we only highlight energies near and below the Coulomb barrier, where the coupled-channels effects are largest.

The lowest dashed curve in Fig. 10 shows the capture cross section obtained from the penetration of the one-dimensional barrier, which is produced by the Coulomb repulsion and the nuclear potential (1) and has a barrier height of 158.5 MeV. The next (solid) curve shows the result one obtains by including all of the neutron transfer couplings discussed in Sec. II. It is seen that these couplings do have an effect on subbarrier fusion, or rather capture. The next curve shows the effect of couplings to one-phonon excitations of the 2^+ and 3^- states in projectile and target. Here the enhancement is much larger. The highest solid curve shows the combined effect of couplings to neutron transfer channels and to one-phonon excitations. The combined effect on the energy shift of the subbarrier capture rate is obviously not additive but somewhat weaker.

Finally, the highest dotted curve was obtained by further including couplings to the mutual excitations of the low-lying surface modes and to the two-phonon excitations of the 2^+ states. This is about the best calculation we can make at present. In fact, the radius for the ion-ion potential that we have used in all of our calculations was originally adjusted, as mentioned in Sec. II A, so that the calculated capture cross section was in reasonable agreement with the measurements. The same calculation has already been illustrated in Fig. 9 over the full range of energies, and it appears to reproduce the capture data quite well. There are, of course, uncertainties both in the data (for example, a 1 MeV uncertainty in the center-of-mass energy [3]) as well as in the calculations due to model assumptions. Quasielastic, charged-particle transfer, for example, may have some effect but it is expected to be smaller than the effect of neutron transfer.

VI. CONCLUSION

Our coupled-channels calculations provide a comprehensive and fairly consistent description of many of the reaction and scattering data that have been measured in ^{58}Ni+^{124}Sn collisions. They describe fairly well not only the one- and two-neutron transfer data and the (inclusive) elastic scattering data, but they also reproduce the sum of the measured fusion and deep-inelastic scattering cross sections that have been measured previously.

Our model calculations have still several shortcomings. They are not consistent with the experimental observations that the centroids of the Q-value distributions move to higher excitation energies and the widths increase with increasing number of neutrons being transferred [8]. Neither do they treat explicitly the deep-inelastic reactions that have been observed. However, it would be very difficult to include these aspects in a realistic way in the coupled-channels approach.

Some of the quasielastic, charged-particle transfer reactions, which we have simulated by a weak imaginary potential, could in principle be included the same way we included the neutron transfer channels. That would be attractive in some respects. One could then avoid the uncertainty of employing the imaginary potential and achieve a more consistent description of all reaction channels, in particular of elastic scattering and capture reactions. The required number of channels would become much larger but we do not expect that the qualitative features of our calculations would change much by such an improvement.

Our calculations show, in particular, that the couplings to the neutron transfer channels do enhance the subbarrier capture rates significantly in ^{58}Ni+^{124}Sn collisions. The enhancement is, however, not as strong as the effect of couplings to low-lying surface modes. Moreover, the combined effect of the two sets of couplings on the energy shift of the subbarrier capture rate is not additive but somewhat weaker.

This work was support by the U. S. Department of Energy, Nuclear Physics Division, under Contract No. W-31-109-ENG-38.

[1] W. S. Freeman, H. Ernst, D. F. Geesaman, W. Henning, T. J. Humanic, W. Kuhn, G. Rosner, J. P. Schiffer, B. Zeidman, and F. W. Prosser, Phys. Rev. Lett. **50**, 1563 (1983).
[2] K. T. Lesko, W. Henning, K. E. Rehm, G. Rosner, J. P. Schiffer, G. S. F. Stephans, B. Zeidman, and W. Freeman, Phys. Rev. Lett. **55**, 803 (1985); Phys. Rev. C **34**, 2155 (1986).
[3] F. L. H. Wolfs, W. Henning, K. E. Rehm, and J. P. Schiffer, Phys. Lett. B **196**, 113 (1987); F. L. H. Wolfs, Phys. Rev. C **36**, 1379 (1987).
[4] R. R. Betts *et al.*, Phys. Rev. Lett. **59**, 978 (1987).
[5] C. N. Pass *et al.*, Nucl. Phys. **A499**, 173 (1989).
[6] W. Henning, F. L. H. Wolfs, J. P. Schiffer, and K. E. Rehm, Phy. Rev. Lett. **58**, 318 (1987).
[7] A. M. van den Berg, W. Henning, L. L. Lee, K. T. Lesko, K. E. Rehm, J. P. Schiffer, G. S. F. Stephans, F. L. H. Wolfs, and W. S. Freeman, Phys. Rev. Lett. **56**, 572 (1986); Phys. Rev. C **37**, 178 (1988).
[8] C. L. Jiang, K. E. Rehm, H. Esbensen, D. J. Blumenthal, B. Crowell, J. Gehring, B. Glagola, J. P. Schiffer, and A. H. Wuosmaa, preceding paper, Phys. Rev. C **57**, 2393 (1998).
[9] A. Winther, Nucl. Phys. **A594**, 203 (1995); **A572**, 191 (1994).
[10] H. Esbensen and S. Landowne, Nucl. Phys. **A492**, 473 (1989).
[11] M. Beckerman, M. Salomaa, A. Sperduto, J. D. Molitoris, and A. DiRienzo, Phys. Rev. C **25**, 837 (1982).
[12] A. M. Stefanini *et al.*, Phys. Rev. C **41**, 1018 (1990).
[13] H. Esbensen and S. Landowne, Phys. Rev. C **35**, 2090 (1987).
[14] H. Esbensen and F. Videbaek, Phys. Rev. C **40**, 126 (1989).
[15] R. A. Broglia and A. Winther, *Heavy Ion Reactions*, Frontiers in Physics Lecture Note Series, Vol. 84 (Addison-Wesley, Redwood City, CA, 1991).
[16] D. G. Fleming, Can. J. Phys. **60**, 428 (1982).
[17] J. Wiggins, R. Brooks, M. Beckerman, S. B. Gazes, L. Grodzins, A. P. Smith, S. G. Steadman, Y. Xiao, and F. Videbaek, Phys. Rev. C **31**, 1315 (1985).
[18] J. M. Quesada, G. Pollarolo, R. A. Broglia, and A. Winther, Nucl. Phys. **A442**, 381 (1985).
[19] K. E. Rehm, C. Beck, A. van den Berg, D. G. Kovar, L. L. Lee, W. C. Ma, F. Videbaek, and T. F. Wang, Phys. Rev. C **42**, 2497 (1990).
[20] C. H. Dasso, G. Pollarolo, and A. Vitturi, Phys. Lett. **155B**, 223 (1985); Phys. Lett. B **179**, 337 (1986).